JOURNAL OF GEOPHYSICAL RESEARCH, VOL. 90, NO. C1, PAGES 987–1004, JANUARY 20, 1985

Aircraft and Satellite Measurement of Ocean Wave Directional Spectra Using Scanning-Beam Microwave Radars

FREDERICK C. JACKSON AND W. TRAVIS WALTON[1]

Laboratory for Oceans, NASA Goddard Space Flight Center, Greenbelt, Maryland

PAUL L. BAKER[2]

Computer Sciences Corporation, Silver Spring, Maryland

A microwave radar technique for remotely measuring the vector wave number spectrum of the ocean surface is described. The technique, which employs short-pulse, noncoherent radars in a conical scan mode near vertical incidence, is shown to be suitable for both aircraft and satellite application. The technique has been validated at 10 km aircraft altitude, where we have found excellent agreement between buoy and radar-inferred absolute wave height spectra.

1. INTRODUCTION

Measurements of the state of the sea, particularly of the directional energy spectrum of the wind-generated waves, if available on a routine basis globally from earth-orbiting satellites, would be of immense value in developing and refining wave models and in improving operational wave forecasts [*Earl*, 1981; *Hasselmann*, 1984]. In addition to the obvious practical value of such data to shipping and the offshore industry, for example, such data must ultimately enhance our understanding of wave physics and upper ocean dynamics, first through the physical implications of the model refinements and tuning the data will likely demand, and second through what may well develop as a more realistic view of the role played by the large waves in transferring energy and momentum to the sea. Closely related to this general problem in air-sea interaction is the problem of interpreting satellite scatterometer data (see papers in April 1982 and February 1983 special issues of *Journal of Geophysical Research*). Recent data suggest a dependence of scatterometer return on the larger-wave slopes, independent of wind speed and stability [*Plant et al.*, 1984]. In addition to aiding in the interpretation of satellite scatterometer data, there is the possibility that, given sufficiently good wave models, satellite wave data may itself be useful in inferring the wind field.

For several years now, we have been endeavoring to develop a microwave radar technique for measuring ocean wave directional spectra that would be suitable for satellite application. Basically, we have been seeking to define an alternative to the coherent imaging radar approach that was adopted for Seasat, the nation's first oceanographic satellite [*Beal et al.*, 1981]. Our motivation has been to find an alternative measurement approach that would at the same time (1) be simpler and less costly, (2) be capable of truly global measurements, and (3) be more accurate.

In this we believe we have been successful. Theoretically, and on the basis of aircraft flight experiments we have determined that such global-scale satellite measurements are feasible. The measurements can be made with relatively simple, noncoherent short-pulse radars operating in a conical scan mode near vertical incidence, $\theta \sim 10°$. No new technological developments are required. Rather, these measurements can be made with existing space-qualified hardware. For example, with some relatively minor modifications such as the addition of a modest-gain scanning antenna, the Seasat altimeter can be adapted to perform these measurements. The measurements are inherently of high resolution spectrally in both wave number and direction, and as we shall see, they will be remarkably accurate as well.

A typical satellite measurement geometry is illustrated in Figure 1. For the assumed satellite altitude of 700 km and incidence angle of 10°, the radius of the scan pattern on the ocean surface is approximately 130 km. A 3-rpm antenna rotation rate is selected as a reasonable compromise between coverage and integration time requirements. The measurement cells (not to be confused with the instantaneous field of view, or antenna "footprint") are roughly 130-km squares situated one on either side of the subsatellite track. Basically, the measurement product consists of two statistically stable estimates of the polar-symmetric vector wave number spectrum, one on either side of the subsatellite track. If less than 180° of look is allowed, then these measurements can be confined to an area considerably smaller than the nominal 130-km square as is evident from Figure 1.

Although the technique we shall be considering employs short-pulse waveforms, it is not in its most fundamental aspect different from the two-frequency technique investigated theoretically by *Alpers and Hasselmann* [1978] and experimentally by *Johnson et al.* [1981]. In both techniques the basic measurement principle is the same. This is the directional selectivity that results as a natural consequence of the phase-front matching of electromagnetic and ocean wave components. The choice of waveforms, and the manner of detection, is however a critical one. *Jackson* [1981] has shown that the narrow band two-frequency technique has, inherently, a very low signal-to-noise ratio (snr) compared to the short-pulse technique. Basically, this is because the sea spectrum is relatively broadband, whereas the two-frequency beat-wave signal is comparatively narrow band. For large footprint dimensions, this results in modulation signal power being detected only in a very narrow spectral band, and consequently, the signal energy is small compared to the fading variance.

Our work differs from that of *Alpers and Hasselmann* [1978]

[1]Now at Engineering Research Center, University of Maryland, College Park.

[2]Now at Computer Technology Associates, McLean, Virginia.

Paper number 4C1190.
0148-0227/85/004C-1190$05.00

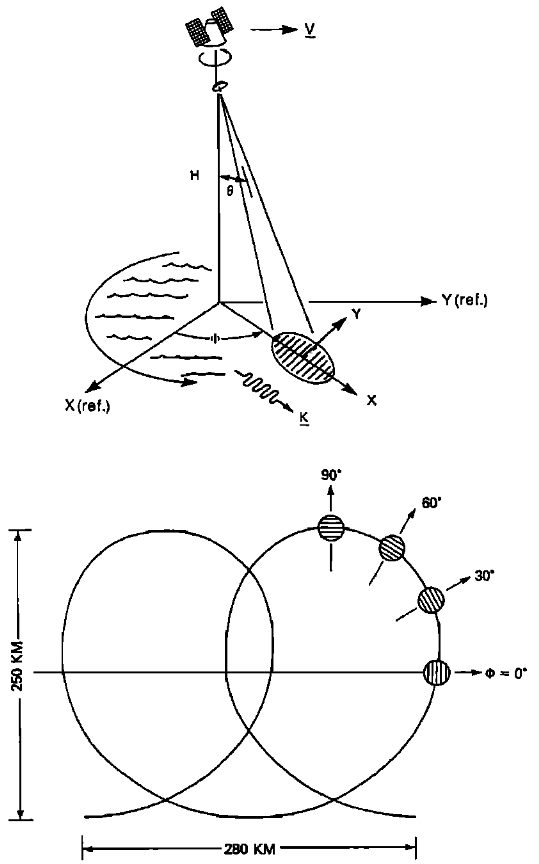

Fig. 1. (*a*) Satellite measurement geometry and (*b*) scan pattern on the ocean surface, 700 km altitude, 10° incidence angle, and 3-rpm scan rate.

in another important respect. This is in the choice of incidence angles. *Alpers and Hasselmann* [1978] were concerned with large-angle measurements, whereas our concern is with small angles of incidence. There are several reasons why we have chosen to study small-angle scatter. First, as should be apparent from the above discussion of the measurement geometry, small angles of incidence are necessary at satellite altitudes in order to keep the scan radius to a minimum. If the nadir angle is too large, the scan pattern on the surface may exceed the scale of homogeneity of the wave field. Second, the reflectivity modulation mechanism in near-vertical backscatter is simpler and more predictable than it is in large-angle backscatter. In the near-vertical, specular backscatter regime the contrast modulation does not depend on the strong—and essentially unpredictable—hydrodynamic modulation of the short Bragg-diffracting water wave by the atmospheric and large-wave flow fields. The modulation mechanism is primarily a geometrical tilting effect, and consequently, it is more amenable to accurate modelling. Another reason for choosing small incidence angles is an obvious one, that the greater cross-section and lower link loss near nadir demands less transmitter power and antenna gain. This is an important consideration in the wide band measurement approach that we are advocating.

In this paper, we present the results of the analysis of the first comprehensive aircraft data set obtained with the Goddard K_u-band short pulse radar. This data set, obtained with the Goddard radar on an extended flight mission in 1978 with a new conically scanning antenna, fairly conclusively demonstrates the validity of the short-pulse, scanning-beam approach to satellite waves measurements. Comparison with several types of wave-recording buoys shows that over a large range of sea conditions (2–9 m wave height), the technique is capable of yielding accurate estimates of the absolute directional height spectrum. In the following section, we will discuss the three major conceptual elements that constitute the measurement technique, namely, (1) the principle of directional selectivity, (2) the modulation mechanism in near-vertical backscatter, and (3) the use of short-pulse waveforms to detect the range reflectivity modulation. The discussion is intended to provide a basic understanding of the measurement technique and to provide such results and formulas as will be found useful in the analysis of the aircraft data in section 4. For a fuller and more detailed theoretical treatment, the reader is referred to *Jackson* [1981]. In section 3, a possible satellite system based on the scanning-beam approach is described.

2. THE MEASUREMENT TECHNIQUE

2.1. *The Principle of Directional Selectivity*

We are concerned with fairly narrow antenna beams in a high-altitude measurement geometry. The relevant geometry is illustrated in Figure 1. The situation desired is one where (1) the antenna footprint is large compared to the scale of the waves, and (2) the curvature of the wavefront is small compared to the directional spread of the waves. Now obviously, if the lateral beam spot dimension is large compared to the scale of the waves, then the waves cannot be resolved in azimuth (short of resorting to synthetic aperture). Rather, the wave contrasts will be averaged laterally across the beam. What is the effect of this lateral averaging? To understand the effect, imagine a Fourier decomposition of the two-dimensional reflectivity field into an angular spectrum of plane contrast waves. (The reflectivity field can be imagined to be that measured by a very high resolution real-aperture imaging radar looking in the same azimuth direction.) Referring to Figure 2, it is apparent that the effect of the lateral averaging is to eliminate or "cancel out" any plane surface contrast wave that is not aligned with the beam direction. Only those surface waves whose phase fronts are "matched" to the electromagnetic (em) phase front can survive the lateral averaging. The effect of the broad footprint is then to isolate or resolve surface contrast wave components whose wave vectors $\mathbf{K} = (K, \Phi)$ are aligned with the beam direction.

The directional resolution is determined by and limited by (1) the finiteness of the beam spot size in azimuth L_y, and (2)

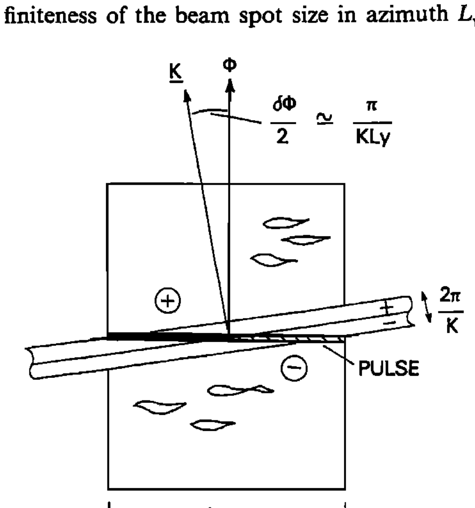

Fig. 2. Illustrating directional selectivity by phase-front matching of em and ocean wave components. For the rectangular illumination pattern illustrated here the angle of the first null is as indicated.

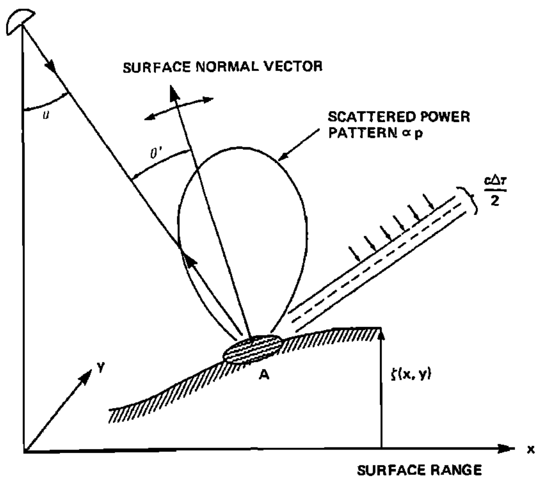

Fig. 3. Simple tilt model of reflectivity modulation.

the curvature of the wave front within the beam spot. If we assume a Gaussian-shaped azimuth gain pattern,

$$G(y) = \exp(-y^2/2L_y^2) \tag{1}$$

then it follows (e.g., from the Fresnel zone solution of *Jackson* [1981]) that the directional resolution $\delta\Phi$, defined as the half power spectral window width in azimuth, is given by

$$\delta\Phi \sim \delta K_y/K = 2\sqrt{2\ln 2}\,[(KL_y)^{-2} + (L_y \cot\theta/2H)^2]^{1/2} \tag{2}$$

where H is the altitude. The first and second terms in (2) derive, respectively, from the finite-footprint and wave-front curvature effects. In our aircraft experiment geometry, $H \sim 10$ km, $\theta \sim 13°$, and $L_y \sim 300$ m (half power width $L_y^* = 2(2 \ln 2)^{1/2}L_y \sim 700$ m). For a typical 200-m water wave, we have $\delta\Phi \sim 17°$. In a typical satellite measurement, $H = 700$ km, $\theta = 10°$, and $L_y = 8.5$ km ($L_y^* = 20$ km), in which case $\delta\Phi \sim 5°$. (Note that the directional resolution quoted by *Jackson* [1981, equation (79)] is in error).

2.2. *The Reflectivity Modulation in Near-Vertical Backscatter*

Near vertical incidence, $\theta \lesssim 15°$, microwave backscatter from the sea occurs by means of quasi-specular reflections from wave facets oriented normal to the radar's line of sight. The average backscatter cross section σ^0 is proportional to the probability density function (pdf) of orthogonal surface slopes satisfying the specular condition for backscatter: $\partial\zeta/\partial x = \tan\theta$; $\partial\zeta/\partial y = 0$. The cross section is given by [e.g., *Valenzuela*, 1978]

$$\sigma^0(\theta, \Phi) = \rho\pi \sec^4\theta\, p(\tan\theta, 0) \tag{3}$$

where p is the slope probability density function (pdf) expressed in the radar's coordinate system, x in the plane of incidence, and ρ is a diffraction-modified normal incidence Fresnel reflectivity [*Brown*, 1978].

Hydrodynamic modulation is a second-order effect in near-vertical backscatter. Consider that, first, for most microwave frequencies, the most strongly forced waves, the gravity-capillary waves, lie under the diffraction limit (about three em wavelengths in the horizontal according to *Brown* [1978]). Thus, they are only weakly sensed, and to the extent that they are, it is via a diffuse diffraction field that can be only very weakly modulated by geometrical tilting. Second, the specular component derives from the entire wave ensemble, including waves on all scales, from the scale of the dominant waves we are seeking to measure down to the scale of the diffraction limit. For this large ensemble of waves, it is reasonable to assume that hydrodynamic forcing and wave-wave interaction effects are of secondary importance. To the extent that hydrodynamic nonlinearities effect the em modulation, they are to be attributed to the entire wave ensemble rather than a particular water wave component. Neglecting second-order effects, the surface can be treated as a free-wave superposition possessing Gaussian statistics. If the large-wave slopes are then assumed to be small compared to the total rms surface slope, the modulation can be modelled by the following linear "tilt model."

The backscatter cross section of a small patch of sea surface of area A (cf. Figure 3) is given by $\sigma = \sigma^0 A$, where the normalized cross section σ^0 is assumed to be the average σ^0 of the sea surface in a tilted reference frame. Thus, if θ' and Φ' are the local incidence and azimuth angles, we suppose that σ^0 (patch) $= \sigma^0(\theta', \Phi')$. For small large-wave tilts δ, the fractional cross section variation is given by

$$\frac{\delta\sigma}{\sigma} \simeq \frac{\delta\sigma^0}{\sigma^0} + \frac{\delta A}{A} \tag{4}$$

The elementary surface area is that area contained in the range interval $c\Delta\tau/2$. To first order in δ, A is given by $A = \Delta y(c\Delta\tau/2) \csc\theta'$. Provided that $\delta \ll \theta$, the local incidence angle can be approximated by $\theta' \sim \theta - \partial\zeta/\partial x$. Thus, to first order in δ it follows that $\delta A/A = \cot\theta\, \partial\zeta/\partial x$. Since the azimuthal dependence of σ^0 is small compared to the θ dependence, it follows that the tilt term $\delta\sigma^0/\sigma^0$ is also proportional to the large-wave slope component in the plane of incidence. From (3),

$$\frac{\delta\sigma^0}{\sigma^0} = -\frac{1}{p}\frac{\partial p}{\partial \tan\theta}\frac{\partial\zeta}{\partial x} + O(\delta^2) \tag{5}$$

The fractional range-reflectivity modulation seen by the radar is $\delta\sigma/\sigma$ averaged laterally across the beam:

$$m(x, \Phi) = \frac{\int G^2(y)(\delta\sigma/\sigma)\, dy}{\int G^2(y)\, dy} \tag{6}$$

The directional modulation spectrum is defined by

$$P_m(K, \Phi) = (2\pi)^{-1} \int \langle m(x, \Phi) m(x + \xi, \Phi)\rangle \exp(-iK\xi)\, d\xi \tag{7}$$

where the angle brackets denote ensemble average. Now let G be given by the Gaussian pattern (1), and consider the limiting case of very large footprints, $KL_y \gg 1$. It is easy to show then that P_m is proportional to the directional slope spectrum as

$$P_m(K, \Phi) = \frac{\sqrt{2\pi}}{L_y}\left(\cot\theta - \frac{\partial \ln p}{\partial \tan\theta}\right)^2 K^2 F(K, \Phi) \tag{8}$$

where F is the two-sided, polar-symmetric height spectrum defined so that the height variance,

$$\langle\zeta^2\rangle = \int_0^\infty \int_0^\pi 2F(K, \Phi) K\, dK\, d\Phi \tag{9}$$

The rms modulation depth, by definition, is given by

$$\mu(\Phi) = \langle m^2(x, \Phi)\rangle^{1/2} = \left[\int_0^\infty 2P_m(K, \Phi)\, dK\right]^{1/2} \tag{10}$$

It should be pointed out that, strictly, the large footprint limiting form is valid only if L_y is much larger than the lateral decorrelation scale of $\partial\zeta/\partial x$. This is equivalent to the condition $KL_y \gg 1$ in the general case of directionally spread seas, but not in the case of unidirectional, long-crested swell. We have encountered such a swell in our aircraft experiment, where the crest length was very long compared to L_y. In such a case a separate calculation must be carried out, one which accounts for the curvature of the em wave front. But as the case we encountered was exceptional among our data, we have neglected to perform such a calculation.

Now it is only consistent at this point to assume that the slope pdf is Gaussian. Indeed, it would be inconsistent to assume otherwise, since the tilt model is predicated on an assumption of free, noninteracting waves, and this can only imply normal statistics. The K_u-band scatterometer data of *Jones et al.* [1977] analyzed by *Wentz* [1977] show in fact that the pdf is nearly normal. More interesting though, the data indicate that the pdf at K_u-band frequencies is very nearly isotropic. This is convenient, as it simplifies the measurement of bi- or multimodal directional spectra, since the sensitivity is independent of azimuth, and no relative weighting of different directional components is required. If the slope pdf is Gaussian and isotropic, then the sensitivity coefficient, the factor of K^2 F in (8), can be written as

$$\alpha \equiv \frac{\sqrt{2\pi}}{L_y}\left(\cot\theta + \frac{2\tan\theta}{\langle|\nabla\zeta|^2\rangle}\right)^2 \tag{11}$$

where $\langle|\nabla\zeta|^2\rangle$ is the mean square wave slope effective at the particular radar operating frequency (diffraction-effective mean square slope).

The linear tilt model solution (8) is identical to the first term in the series expansion of the geometrical optics solution obtained by *Jackson* [1981]. The second-order terms consist of a em and a hydrodynamic (hydro) term. The two terms are of comparable magnitude, both scaling as the large-wave steepness $\delta_0 \equiv K_0\langle\zeta^2\rangle^{1/2}$ to the fourth power. The em term is independent of hydrodynamic nonlinearity and arises in scattering from a normally distributed sea surface. The hydro term is due to the non-Gaussian statistics associated with hydrodynamic nonlinearity, and is given in terms of various third moment statistics in wave height and slope. Since these statistics scale with δ_0 (see *Jackson* [1981]; also *Huang and Long* [1980]), the result is that both em and hydro terms scale as δ_0^4. The calculations of the second-order em term carried out by Jackson indicate that, first, the term is generally small, and second, that the least harmonic distortion occurs in the neighborhood of 10° incidence. The smallness of the second-order terms requires that the following inequalities should be satisfied:

$$\delta_0 \cot\theta \ll 1 \tag{12a}$$

$$\frac{\delta_0 \tan\theta}{\langle|\nabla\zeta|^2\rangle} \ll 1 \tag{12b}$$

If (12*a*) is violated seriously, an obvious consequence is that the phase front, or pulse, may intersect the surface at more than one point. A less extreme but more general consequence of violating (12*a*) is the confounding of the surface range coordinate with the wave height. The range coordinate will suffer a displacement $\delta x = \zeta \cot\theta$. The net result will be a dispersion of the range coordinate by an amount $\langle\zeta^2\rangle^{1/2} \cot\theta$. This dispersion will represent a limit to the smallest wavelengths observable by this technique. Since $\langle\zeta^2\rangle^{1/2} = \delta_0/K_0$, it follows that the upper limit on wave number as a function of the peak wave number is of the order of

$$K_{max}/K_0 \simeq (\delta_0 \cot\theta)^{-1} \tag{13}$$

For example, if $\theta = 10°$ and $\delta_0 = 0.05$ (fully aroused seas), then $K_{max} \sim 3.5K_0$. In steep developing seas, $\delta_0 \sim 0.1$, in which case $K_{max} \sim 1.75K_0$. To illustrate the nature of the spurious response associated with the violation of (12*b*), take the extreme case of swell under calm conditions. Obviously, if $\tan\theta > \delta_0$ then no backscatter occurs, since there are no wave slopes satisfying the specular condition. If $\tan\theta < \delta_0$, the backscatter will now occur in periodically spaced bursts at points on the swell profile satisfying the specular condition. The backscatter will look like a string of delta functions, and will bear little resemblance to the swell profile save in its periodicity. Clearly, for the measurement to have decent fidelity (to the slope spectrum) there must be sufficient small-scale roughness, or in other words, a sufficient density of specular points. Practically, this means that the local wind speed should be in excess of several meters per second.

Some guide to the selection of the "best" incidence angle may be had by the following. Assume that the inequalities (12) carry equal weight, that is, assume that the consequences of violating (12*a*) and (12*b*) are equally undesirable. Then we can minimize the sum (12*a*) + (12*b*) with respect to θ. This yields $\tan\theta = \langle|\nabla\zeta|^2\rangle$. For example, if the wind speed is 10 m s^{-1}, then by using (33) we get $\theta = 10°$. More work along the lines established in *Jackson* [1981] is required to get a better idea of what is really the best angle for minimizing the measurement nonlinearities. Unfortunately, the aircraft data are of little or no use here. This is because at the relatively low aircraft altitudes, the elevation beamwidth must be fairly broad in order to generate a sufficiently large beam spot for wave number resolution. In our aircraft experiment geometry, the 10° elevation beamwidth makes it virtually impossible to establish the optimal angle since the likely range of θ lies within the beamwidth.

2.3. *The Short-Pulse Technique*

In principle, the range reflectivity modulation spectrum $P_m(K, \Phi)$ can be measured by either short-pulse or two-frequency techniques. However, as shown by *Jackson* [1981], the narrowband two-frequency technique has, inherently, a poor measurement snr (signal-to-noise ratio) compared to the short-pulse technique. This is due to the use of narrowband waveforms that completely fill the beam. The analysis bandwidth δK in this case is equal to the reciprocal of the range footprint dimension—the "record length." Hence the snr $\equiv P_m(K)\delta K$ will necessarily be small when the footprint dimension is large. Since $P_m \propto L_y^{-1}$ and $\delta K \propto L_x^{-1}$, it follows that the two-frequency snr is inversely proportional to the footprint area as noted by *Alpers and Hasselmann* [1978].

In the short-pulse technique, wide bandwidth, short pulses are used to resolve the wave structure in range [*Tomiyasu*, 1971]. Backscattered pulses are integrated in surface-fixed range bins, and the range modulation spectrum is computed digitally from the observed sample of the range modulation $m(x, \Phi)$. For narrow pencil beams, the curvature of the wave front can be neglected, and the surface range can be taken to be a linear function of the signal delay time τ. If the motion of the platform is for the moment ignored, then

$$x = c\tau/(2\sin\theta) \tag{14a}$$

where c is the speed of light, and where the origin is taken to be the beam spot center. The surface range resolution is given by

$$\Delta x = c\Delta\tau/(2\sin\theta) \tag{14b}$$

where $\Delta\tau$ is the pulse length (compressed if coded waveform).

The coherency of the radiation results in random signal fading akin to the speckle observed when a coherent laser illuminates a "rough" surface such as an ordinary piece of bond paper. For any randomly rough surface, the scattered field (outside, perhaps, of the forward specular direction) will have approximately normal statistics. This follows if the field scattered from any elementary range interval dx is the resultant of a superposition of scattered waves from a "large number" of scatterers distributed randomly in range over several em wavelwngths. Thus the resultant phasor $a \exp(i\phi) = \sum a_j \exp(i\phi_j)$ $(x_j \in dx)$ is approximately normally distributed, and the amplitude is Rayleigh-distributed [*Beckmann and Spizzichino*, 1963]. In the absence of large-wave modulation, the reflectivity density of the surface can be modelled as a Gaussian noise process of the form $dA/dx = (\sigma^0/\delta x_c)^{1/2} a(x) \exp[i\phi(x)]$, where δx_c is a coherency distance (typically on the order of several em wavelengths) and $a(x)$ is a unit amplitude Rayleigh process. The large-wave structure affects a modulation of the basic reflectivity density dA/dx. If the reflectivity modulation is denoted g, $\langle |g|^2 \rangle \equiv 1$, then the impulse response of the surface proportional to $g(x)\, dA/dx$. The backscatter of a finite-duration transmitted pulse is given by the convolution of the pulse waveform with the surface impulse response. Thus, if $e_0'(\tau) \equiv e_0(x)$ is the pulse waveform, then the backscattered field e_s as a function of the surface range is given by, for any ith transmitted pulse,

$$e_{si}(x) = C \int e_0(x - x') g(x')\, dA_i(x') \tag{15a}$$

where C is a constant, and where, for simplicity, the azimuth dependence is taken implicitly and the effect of the finite gain pattern is ignored. The coherency distance δx_c is assumed to be small compared to the surface range resolution $\Delta x = c\Delta\tau/(2 \sin\theta)$. In the limit as $\delta x_c \to 0$, dA/dx becomes a Gaussian white noise process described by a delta-function autocovariance,

$$\langle dA(x)\, dA^*(x') \rangle = \sigma^0 \delta(x' - x)\, dx\, dx' \tag{15b}$$

where the asterisk denotes the complex conjugate. From a well-known result for Gaussian-distributed random variables, it follows that the fourth-moment function is given by

$$\begin{aligned}\langle dA(x)\, dA^*(x')\, dA^*(x'')\, dA(x''') \rangle &= (\sigma^0)^2 [\delta(x - x')\delta(x'' - x''') \\ &\quad + \delta(x - x'')\delta(x' - x''') + \text{sum frequency term}] \\ &\quad \cdot dx\, dx'\, dx''\, dx''' \end{aligned} \tag{15c}$$

where the sum frequency term can be neglected, since it is not passed by the detector. If the detected power $W_i \equiv |e_{si}|^2$, then it follows from (15*b*) that the average backscattered power is given by

$$W_0 = \langle W_i \rangle = C^2 \sigma^0 \int |e_0(x)|^2\, dx \tag{16}$$

Similarly, by using (15*c*) one can compute the autocovariance and the spectrum of the backscattered power. For large beam extents L_y, the reflectivity modulation will be weak, in which case the power reflectivity modulation can be modelled as

$$|g|^2 = 1 + m \tag{17}$$

where $\langle m(x) \rangle \equiv 0$. Computing the spectrum of the backscattered power in the individual pulses $P_i(\mathbf{K})$ by taking the Fourier transform of the autocovariance of the normalized backscattered power W_i/W_0 one finds

$$P_i(K, \Phi) \simeq \delta(K) + R(K) P_m(K, \Phi) + [1 + \mu^2(\Phi)] P_w(K) \tag{18a}$$

where $\delta(K)$ represents the dc (antenna pattern term), and where $R(K)$ and $P_w(K)$ represent, respectively, the pulse roll-off, or response function, and the power fading spectrum. The approximation in (18*a*) stems from an approximation in the fading spectrum term, the error in which is negligible provided that the dominant wavelength is large compared to the range resolution. If $E_0(K)$ denotes the Fourier transform of $e_0(x)$, then

$$\begin{aligned} R(K) &= \frac{\left[\int E_0(K') E_0^*(K' - K)\, dK'\right]^2}{\left[\int |E_0(K)|^2\, dK\right]^2} \\ P_w(K) &= \frac{\int |E_0(K')|^2 |E_0(K' - K)|^2\, dK'}{\left[\int |E_0(K)|^2\, dK\right]^2} \end{aligned} \tag{18b}$$

For a Gaussian pulse shape of half power width $\Delta\tau = (2\Delta x/c) \sin\theta$, one finds

$$\begin{aligned} R(K) &= \exp(-K^2/2K_p^2) \\ P_w(K) &= \frac{\exp(-K^2/2K_p^2)}{\sqrt{2\pi}\, K_p} \end{aligned} \tag{18c}$$

where

$$K_p \equiv \frac{2\sqrt{\ln 2}}{\Delta x}$$

Thus the fading spectrum level is inversely proportional to the pulse bandwidth; if the entire bandwidth is used for range resolution, then it follows that P_w is proportional to the range resolution Δx. If the signal-to-noise ratio (snr) is defined as the ratio of the signal spectrum RP_m to the fading noise spectrum P_w, then the individual pulse snr is (neglecting $\mu^2 \ll 1$)

$$\text{snr}_i = \frac{2\sqrt{2\pi \ln 2}}{\Delta x} P_m(\mathbf{K}) \tag{19}$$

An integration of N independent pulses will serve to reduce the fading variance by a factor of N^{-1}. Provided that the integration time is short (<1 s) the surface can be regarded as essentially frozen, and the platform motion can be compensated for, for example, by simply delaying or advancing the trigger on the sample gates according to the line-of-sight relative speed between the platform and the surface. The N-pulse average can be expressed as

$$W_N(\tau) = N^{-1} \sum_{i=1}^{N} W_i(\tau + \dot{\tau} t_i) \tag{20}$$

where the rate of change of signal delay $\dot{\tau} = -(2V/c) \sin\theta \cos\Phi$. Since the fading spectrum level is reduced by a factor of N, the N pulse average snr becomes

$$\text{snr} = N \times \text{snr}_i \tag{21}$$

The number of independent pulses depends on the pulse repetition frequency (PRF); the Doppler bandwidth B_d, and the integration time T_{int}. If the PRF > $2B_d$, the signal is essentially continuously sampled and hence $N = B_d T_{\text{int}}$. If the PRF $\ll B_d$, then the individual pulses are independent, in which case $N =$ PRF $\times T_{\text{int}}$. The Doppler bandwidth is determined by the interference rate of waves backscattered from the lateral extremities of the range resolution cell. From elementary considerations, or from equation (72) in *Jackson* [1981],

$$B_d = (2V/\lambda)\beta_\phi|\sin \Phi| \tag{22}$$

Here B_d is the half power, postdetection Doppler spread in hertz, λ is the em wavelength, and $\beta_\phi \equiv (L_y{}^*/H) \cos \theta$ is the half power azimuth beamwidth.

The measurement integration time is limited by the azimuth scan rate which in turn is driven by coverage requirements. The integration time should not be longer than the time it takes to move one footprint dimension. The modulation signal can only be built up coherently when the radar is viewing the same portion of the surface. When the beam moves to view a new, statistically independent patch of sea, the range modulation signal will evolve randomly, and further integration will proceed in an incoherent fashion, not only with respect to the scintillation or fading noise, but with respect to the modulation signal as well. Thus both P_m and P_w will be driven down as N^{-1}. Thus, as the beam moves to view a new piece of the surface, the signal strength goes down as $1/T_{\text{int}}$, while the snr approaches an asymptotic value. Since the antenna rotation is generally more rapid than the beam's translation, the azimuth scan rate determines the choice of integration time. Let us arbitrarily require that the beam move no more than one half of its azimuth dimension. Then the integration time is set by

$$T_{\text{int}} \leq \Delta\Phi/2\dot{\Phi} = \beta_\phi \csc \theta/2\dot{\Phi} \tag{23}$$

An interesting consequence of (23) is that the snr is independent of the footprint dimensions and hence of the antenna gain. This follows since the integration gain $N \propto T_{\text{int}} \propto L_y$, while the signal spectrum $P_m \propto L_y{}^{-1}$. Thus, while the azimuth beamwidth affects the modulation signal strength (weakly as $L_y{}^{-1/2}$) it does not affect the measurement snr.

The number of degrees of freedom (DOF) in a measurement of $P_m(\mathbf{K})$ is determined by the number of elementary wave number bands $\delta K \sim 2\pi/L_x{}^*$ contained in the spectral estimate. For example, consider an analysis with 25% resolution. Then the DOF of the estimate is given by [*Blackmann and Tukey*, 1958]

$$\text{DOF} \sim 2(0.25)/\delta K \sim KL_x{}^*/4\pi \tag{24}$$

For example, if $L_x{}^* = 20$ km and $K = 2\pi/200$ m, then the DOF ~ 50.

3. A SATELLITE SYSTEM

It is a simple matter to show that these measurements can be made with a modified Seasat-class radar altimeter. The pertinent Seasat altimeter characteristics are as follows [*Townsend*, 1980]: frequency: 13.5 GHz; pulse type: linear FM, 1000:1 pulse compression; pulse length: 3.2 ns compressed; peak power: 2.0 KW; PRF: 1000 Hz; detection: noncoherent square law.

One can imagine modifying the Seasat altimeter so that it can perform a dual function, first as an altimeter per se, and second as a "directional wave spectrometer." In the conventional altimeter mode, mean altitude and wave height are determined from the delay time and broadening of the leading edge of the averaged return of nadir-directed pulses [cf. *Jackson*, 1979]. There are several ways whereby transmitted pulses may be shared between the instrument's nadir altimeter mode and off-nadir spectrometer mode, for example, by power dividing or time sharing. Modification would entail the addition of a separate receiving section (post IF) and microprocessor as well as a separate rotating antenna. Pulse tracking, integration and spectral analysis functions would be incorporated in the separate microprocessor. As an example, let us consider adding a 1-m-diameter, 3-rpm rotating antenna to the existing instrument (or its counterpart). If we assume a 700-km satellite altitude and 10° nadir angle, then the measurement geometry is that of Figure 1, and the relevant measurement parameters are as follows: velocity: $V = 7$ km s^{-1}; beamwidth: $\beta_\theta = \beta_\phi = 1.6°$; spot size: $L_x{}^* \sim L_y{}^* = 20$ km, ($L_x \sim L_y = 8.5$ km); rotation rate: $\dot{\Phi} = 360°/20$ s; range resolution: $\Delta x = 2.8$ m (from (14*b*)); Doppler bandwidth: $B_d = 18$ $|\sin \Phi|$ KHz (from (22)); integration time: $T_{\text{int}} = 0.26$ s (from (23)). The PRF equals B_d at $\Phi \sim 3°$ of forward or aft. For most azimuths the PRF $\ll B_d$, so that the number of independent samples is given by

$$N = \text{PRF} \times T_{\text{int}} = 260 = +24 \text{ dB}$$

For illustrative purposes, let us assume a Phillips' cutoff spectrum with a $\cos^4$ spreading factor:

$$F(K, \Phi) = 0.005(4/3\pi) \cos^4 (\Phi - \Phi_0)K^{-4} \qquad K \geq K_0$$

$$F(K, \Phi) = 0 \qquad K \leq K_0$$

Assume a 200 m water wavelength and upwave/downwave looks. Let the mean square slope as a function of wind speed be given by (33) and let $U = 10$ m s^{-1}. Then we have (cf. (8), (10), (11), and (21)):

$$P_m = (2.95 \times 10^{-4} \text{ m}^{-1})(5.67 + 9.53)^2(2.15 \text{ m}^2) = 0.15 \text{ m}$$

$$\mu = 10\%$$

$$\text{snr} = 260 \times 0.22 = +18 \text{ dB}$$

The directional resolution given by (2) is $\delta\Phi = 4.7°$; but this assumes no rotation of the beam. Since the beam moves about 5° during the integration time, the actual resolution will be approximately 7°. We have already calculated the DOF in the last section: DOF ~ 50. At 10° incidence, $\sigma^0 \sim +5$ dB and is very nearly independent of wind speed. A link equation assuming 3 dB in losses and a noise factor of $F = 6$ dB gives a signal-to-thermal-noise ratio of $+6$ dB. Thus thermal noise is not a problem, even if half the transmitter power is shared with the altimeter mode.

The spectrometer mode does not require the full pulse compression. For example, a partial compression of the chirped waveform to 20 ns (17.3 m surface range resolution) would be quite adequate. The excess bandwidth, of course, is still useful for reducing the fading variance. With 20 ns resolution, something like 1024 sample gates would adequately sample the return (17.7 km of surface range). The spectrometer mode data can be merged with the altimeter mode data stream in a way that is compatible with the existing instrument's data system. For example, the spectrometer data might consist of fifty-eight 6% bandwidth spectral estimates covering the wavelength range 50–1000 m output at a nominal four frames per second. These data can easily be merged with the altimeter data without exceeding the 10 kbit/s^{-1} data rate of the existing system. Thus, on-board recording and hence fully global coverage is possible.

4. AIRCRAFT VALIDATION

4.1. *The Fall 1978 CV-990 Mission*

The Goddard K_u-band short-pulse radar was built up from the GEOS 3 satellite altimeter breadboard obtained from

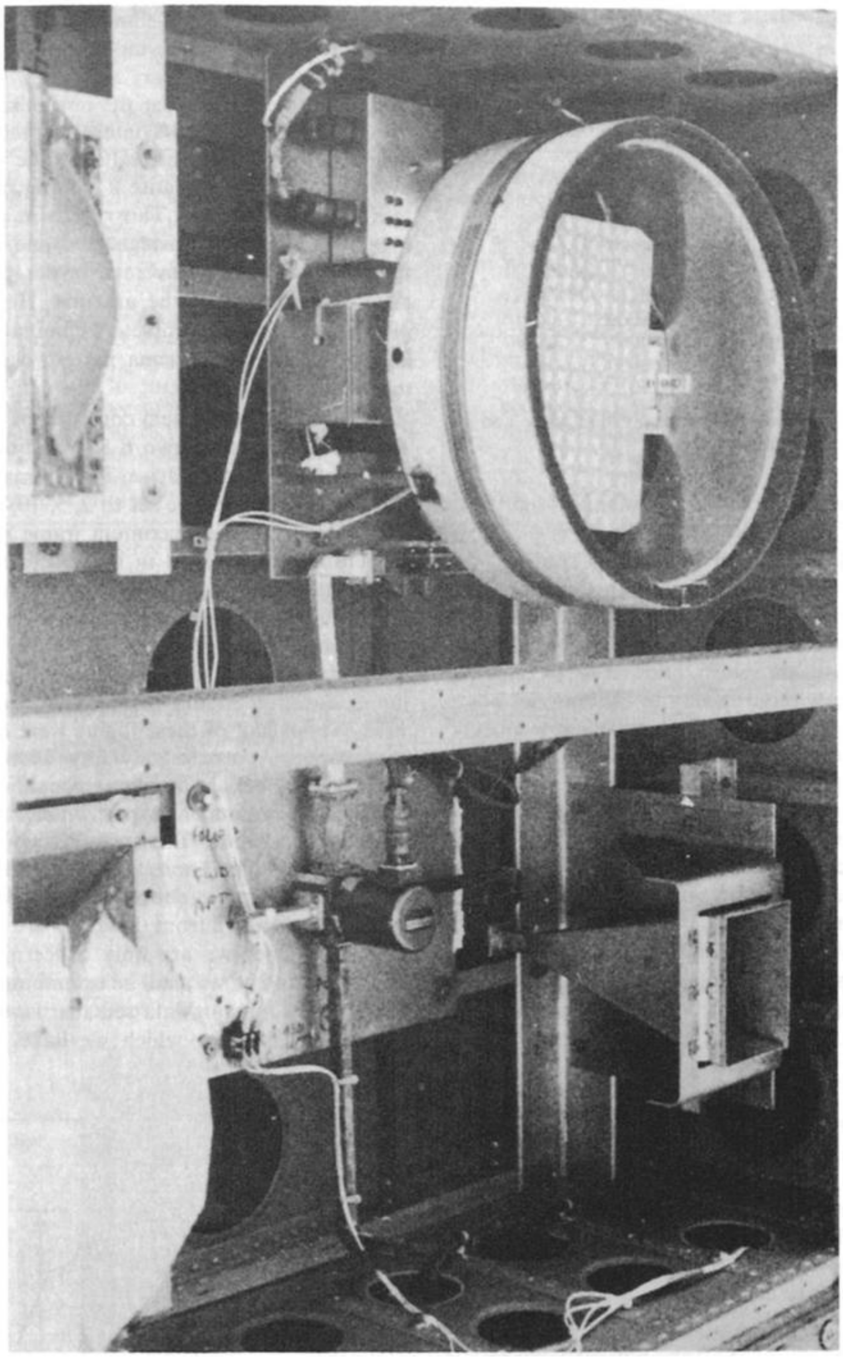

Fig. 4. Antennas mounted in the CV-990 instrument "sled." View is upward, looking into the sled with the radome cover removed. The rotating antenna is surrounded by a cylindrical baffle. The nadir-pointing horn antenna is connected to the rotary antenna by a wave guide switch. The other antennas shown belong to the SMMR simulator microwave radiometer.

General Electric in 1974, and it shares the following characteristics with the spacecraft instrument: frequency: 13.9 GHz; pulse type: linear FM, 100:1 pulse compression; pulse length: 12.5 ns compressed; peak power: 2.5 KW; PRF: 100 Hz; detection: noncoherent square law.

Prior to 1978, the radar was flown on several aircraft missions with fixed-azimuth, variable elevation antennas. A description of the Goddard radar as it was configured in 1975 is given by *Le Vine et al.* [1977]. A major breakthrough in our program occurred in 1978 when we had an opportunity to fly piggyback, free of charge, on the 1-month-long, Convair-990 Nimbus 7 underflight mission. For this mission, one of the fixed-azimuth printed-circuit antennas was modified (by sawing it in half) and adapted to an azimuth scan. Also, the data system was redesigned to allow continuous recording at the full PRF. Figure 4 shows the rotating antenna installed in the CV-990's instrument "sled." It is shown surrounded by a cylindrical baffle which was designed to protect a neighboring radiometer from possible RFI. Also shown in Figure 4 is a 12° × 12°, nadir-directed rectangular horn antenna, which served in our instrument's "altimeter" mode. The nadir horn and rotating antennas are shown connected by a waveguide switch; this switch could be activated by a mode-change command from the radar's control panel in the aircraft cabin. The

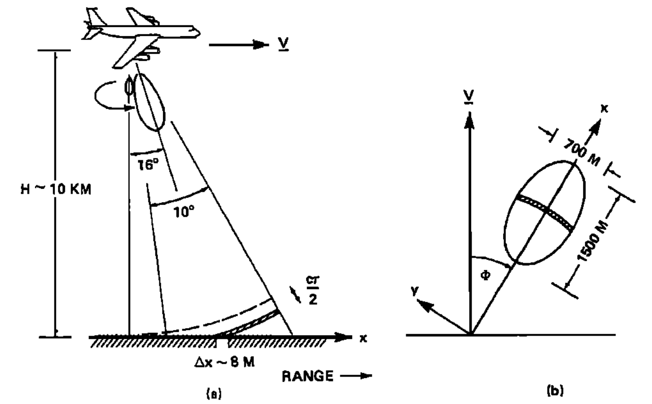

Fig. 5. Aircraft measurement geometry (*a*) elevation view and (*b*) plan view.

rotating antenna characteristics are as follows: boresight incidence angle, $\theta_0 = 15.8°$; azimuth beamwidth, $\beta_\phi = 4°$; elevation beamwidth, $\beta_\theta = 10°$; rotation rate, $\Phi = 6$ rpm.

The boresight angle was chosen so that an elevation sidelobe at 15.8° to the main-beam axis would be directed toward nadir. The return from the sidelobe, which was recorded in the same frame as the main-beam return, allowed us to calculate the range on the surface without having to calibrate for absolute time delay. This is important in the relatively low-altitude (10 km) aircraft geometry where a rather broad elevation beamwidth is required to generate a large enough range footprint extent for wave number resolution. Thus in the aircraft geometry, wave-front curvature in the elevation plane is not negligible, and if not properly accounted for, the curvature will result in a considerable dispersion of the surface wave number. If τ is the time elapsed from the time of the nadir sidelobe return, then given the aircraft altitude from the plane's operational altimeter, the surface range x as measured from the nadir point can be calculated according to the equation

$$x^2 + H^2 = (c\tau/2 + H)^2 \tag{25}$$

Of course, in the satellite measurement geometry, we can linearize (25) to get (14). The aircraft measurement geometry is illustrated in Figure 5. At the nominal aircraft altitude of 10 km, the footprint dimensions are $L_x^* = 1500$ m and $L_y^* = 700$ m approximately. Because of the rapid roll-off of σ^0 with θ, the backscattered power peaks inward of the boresight angle. Generally, the peak return occurs in the vicinity of 13° incidence. The metallic baffle, and the poor radome environment in general, spoiled the gain pattern to such an extent that we have not attempted to measure σ^0 either as a function of elevation or azimuth angle. Figure 6 is an example of the (azimuthally averaged) average backscattered power profile. The large $\sim 3°$ ripple near the beam axis caused by diffraction by the baffle is obvious. The poor gain pattern is unfortunate as, ideally, we want to estimate the tilt model sensitivity term $\partial \ln p/\partial \tan\theta$ directly from the observed cross-section roll-off. The gradient of the slope pdf and mean square slope are internal parameters of the measurement; yet, in the analysis to follow we shall have to rely on external parameters in order to calculate the tilt model sensitivity α. That is, we will have to use a mean relationship between the mean square slope and the buoy-observed wind speed in order to verify the prediction of the tilt sensitivity coefficient (11). In addition to making it difficult to estimate the mean square slope parameters, the gain pattern anomaly also will contaminate the measured spectra. While in principle the gain pattern, including any anomalous structure, is eliminated in the normalization procedure for estimating the modulation, in practice, aircraft motions and the particular algorithm used to estimate the average power pattern for the normalization combine to produce spurious spectral content, especially at the lower frequencies. Particularly, aircraft attitude variations over the duration of the file will cause a shifting of the pattern and pattern anomaly position. This results in an average power estimate which may be misregistered and/or smeared relative to the actual (ensemble) average power profile for a particular azimuth and turn of the antenna. Hence the normalization procedure may not completely eliminate the antenna pattern, and low-frequency antenna pattern energy may contaminate the measured spectra.

The digital data system consisted of a high-speed waveform sampler (Biomation), two 6 K-byte buffers, and a high-speed (75 ips) 1600 bpi tape drive. The Biomation sample gates were selectable and could be set to 2, 5, 10, or 20 ns. Quantization was 6 bits and the maximum frame size was 1024 samples. Generally, we recorded in the spectrometer mode at a 5- or 10-ns rate, taking 512 samples at the full PRF. Shaft encoder and other housekeeping data were recorded in the first two tape tracks.

The fall 1978 mission took in 19 flights of approximately 5 hours duration in the period October 24 to November 19, 1978. About half of these flights were over ice, the remainder over water. Approximately fifty 2400-ft tapes were written with ocean backscatter data; roughly half these data were taken in the instrument's spectrometer mode, the remainder in the altimeter mode. The spectrometer files are by and large 1–2 min long. The 1-min files, amounting to only six antenna rotations, are a bit short on equivalent DOF and, consequently, the spectra from these files are noisy.

In this paper we are only concerned with validating the technique, and so we shall be examining only a small subset of the fall 1978 mission data set; that is, we shall only be examining those files for which we have corroborative "surface

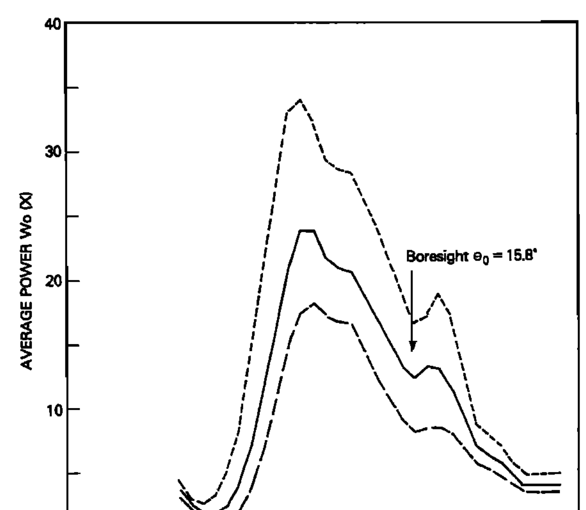

Fig. 6. Azimuthally averaged, average backscattered power profile, tape 37/file 1. The upper and lower dashed curves represent respectively the average maximum and minimum values over 360° of azimuth.

TABLE 1. Fall 1978 Mission Surface Truth Data Summary (Spectrometer Mode)

Flight	Tape/ File	Date, 1978	GMT Start	GMT Stop	Mean Latitude, deg/min	Mean Longitude, deg/min	Altitude, km	Heading, °T	Buoy ID[a]	GMT	H_s, m	Wind Speed,[b] ms^{-1}	Wind Direction,[b] °T	Colocation Distance km	Colocation Time hours	Note
6	27/1	Oct. 30	1801:13	−04:32	71.35 N	18.02 E	5.7	248	TROMSO	1725	4.2	10.1	330	3	0.6	*c*
7	29/1	Nov. 1	0840:12	−42:20	72.38 N	23.10 E	9.5	051	TROMSO	0825	2.4	4.6	240	100	0.3	*c*
9	36/1	Nov. 3	0811:45	−18:32	71.16 N	18.09 E	9.4	247	TROMSO	0831	9.4	18.4	280	13	0.3	
10	45/2	Nov. 6	0950:00	−50:45	71.12 N	18.56 E	9.5	356	TROMSO	0818	3.1	11.5	190	11	1.5	
11	45/3	Nov. 6	0954:30	−55:30	71.46 N	19.14 E	9.5	011	TROMSO	1118	2.8	11.5	190	10	1.4	
									TROMSO	1132	2.3	11.5	190		1.6	
17	85/10	Nov. 17	0001:30	−02:30	42.14 N	131.45 W	9.6	071	EB-16	0000	2.2	7.9	325	14	0.0	
17	86/4	Nov. 17	0036:49	−37:45	45.11 N	130.45 W	9.5	345	EB-21	0000	1.9	6.1	009	29	0.6	
17	86/6	Nov. 17	0049:15	−50:15	45.53 N	129.56 W	9.5	091	EB-21	0000	1.9	6.1	009	83	0.8	
18	89/2	Nov. 17	2135:30	−36:30	50.00 N	145.05 W	9.3	267	PAPA	2104	3.5	8.8–12.9	130	6	0.5	*d*
18	89/3	Nov. 17	2142:45	−44:15	50.10 N	145.35 W	4.5	96	PAPA	2138	3.3	8.8–12.9	130	42	0.0	*d*
18	90/7	Nov. 18	0000:30	−01:30	46.18 N	131.31 W	8.4	134	EB-21	0000	1.3	5.7	189	41	0.0	*e*
18	90/9	Nov. 18	0007:00	−07:46	45.52 N	130.27 W	8.4	104	EB-21	0000	1.3	5.7	189	14	0.1	*e*
19	91/6	Nov. 19	2026:40	−27:40	45.36 N	131.37 W	8.7	232	EB-21	2100	4.2	14.4	003	65	0.6	
19	94/2	Nov. 19	2315:40	−17:14	41.51 N	128.55 W	8.7	128	EB-16	2400	4.0	10.3	333	119	0.7	

[a]TROMSO = Waverider buoy, weather station Tromsoflaket, 71.5°N, 19.0°E.
EB-16 = NOAA data buoy 46002, 42.5°N, 130°W.
EB-21 = NOAA data buoy 46005, 46.0°N, 131°W.
PAPA = NOAA pitch-roll buoy, weather station PAPA, 50.0°N, 145.0°W.
[b]Wind speed and direction at nearest 3-hourly reporting time (no height or stability corrections applied).
[c]Unresolved data problem (possibly high A/D bias level).
[d]Wind speed = 8.8 ms^{-1} at 2138Z; 12.9 ms^{-1} at 2029Z.
[e]Unidirectional, monochromatic swell—equation (8) not applicable; see text.

truth." Table 1 is a summary of the surface truth data set (spectrometer mode). This data set consists of overflights of three types of wave-recording buoys, including two NOAA data buoys (N.E. Pacific), a Waverider (Norwegian Sea), and a pitch-roll buoy (N.E. Pacific). Colocation was generally within 100 km spatially and within 1 h temporally.

4.2. *Data Analysis*

The digital flight tapes were reformatted and compressed by averaging three consecutive pulses. Also, the spectrometer mode data were standardized to 10 ns resolution. Figure 7 is an example of the backscatter data contained on the reformatted tapes. The figure shows 1500 pulse returns, intensity-coded and stacked vertically, on a CRT display. These (essentially raw) data were further processed on a general purpose computer as follows:

1. The equally spaced array in time $W_i(m\Delta\tau)$, $m = 1, 2, \cdots, 512$, (where now the subscript i stands for a three-pulse average) is converted to an equally spaced array in surface range $W_i(m\Delta x)$, $m = 1, 2, \cdots, 512$, according to (25), where the

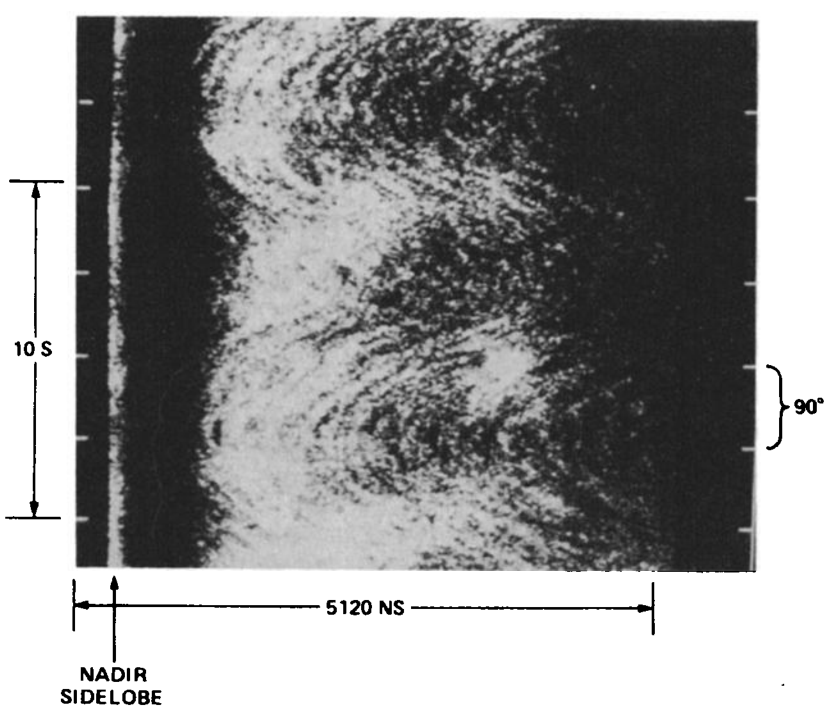

Fig. 7. CRT display of 3-pulse average backscatter data. The sample gate setting is 10 ns and the frame size is 512. The display represents 512 consecutive three-pulse averages stacked vertically. The tic marks are placed every 250 pulses, or, equivalently, every 90° of antenna rotation. The S pattern is the result of antenna rotation combined with aircraft motion.

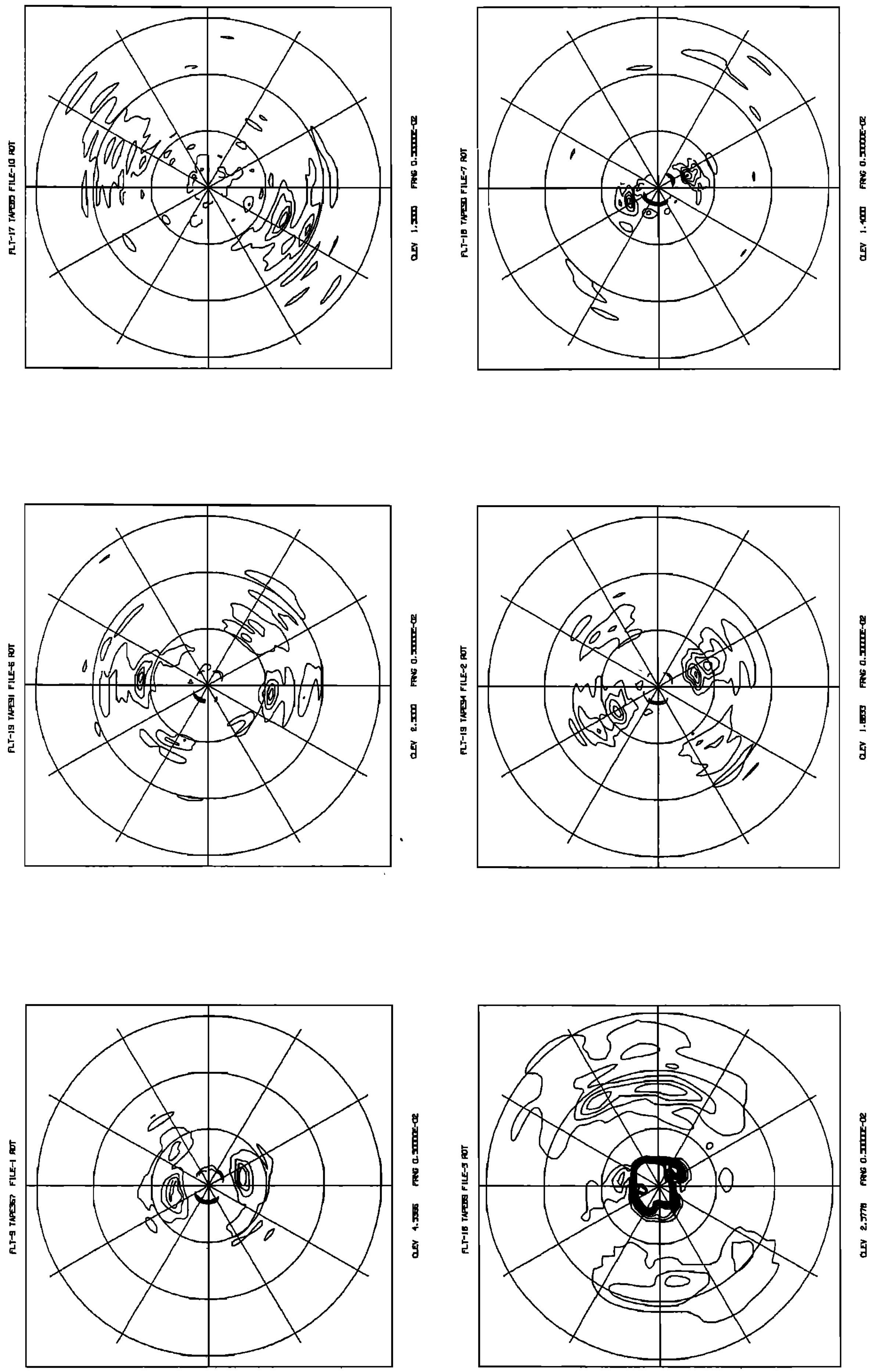

Fig. 8. Polar contour plots of the (one-sided) directional spectra $4\pi P_{42}(K, \Phi)$ in units of meters. Top of the figures is 0° radar azimuth = aircraft heading. The wave number rings are spaced every 0.005 cpm (first ring, 200 m wavelength, second 100 m, and third 66.7 m). The labeled contour level (CLEV) increments are low by a factor of 2; they should read for (*a*) tape/file = 36/1, CLEV = 9.08 m, (*b*) tape/file = 91/6, CLEV = 5.00 m, (*c*) tape/file = 85/10, CLEV = 3.00 m, (*d*) tape/file = 89/3, CLEV = 5.16 m, (*e*) tape/file = 94/2, CLEV = 3.76 m, and (*f*) tape/file = 90/7, CLEV = 2.8 m.

epoch $\tau = 0$ is determined from the location of the nadir sidelobe return. The nominal surface range resolution $\Delta x = 8.1$ m at 13° incidence; however, it was more convenient to array the data in equally spaced 12 m surface range bins (i.e., for the high-altitude 8–10 km data; for the low-altitude 4–6 km data, the bin width is reduced to 6 m).

2. The geometrically corrected data are then subjected to two algorithms. In the first, no motion correction is applied; the data are smoothed in range, and averaged over the several rotations of the antenna. This produces an estimate of the average backscattered power $W_0(x, \Phi)$. In the second algorithm, a motion compensation is applied. That is, the consecutive three-pulse arrays $W_i(m\Delta x)$, $i = 1, 2, \cdots$, are transformed according to $x \leftarrow x + Vt_i \cos \Phi$ using an input aircraft speed. An integration time $T_{\text{int}} = 0.42$ s is chosen to correspond to 15° of antenna rotation (10-s rotation period). Since the PRF = 100 Hz, the number of pulses integrated is $N = 42$. Since the sea-Doppler spread is generally greater than 100 Hz, these pulses are independent for all azimuths, including forward and aft looks. The amount of motion compensation varies from zero for broadside looks (90°) to ca. 80 m = 200 m/s × 0.4 s in the forward and aft (0° and 180°) look directions. The 15° of rotation is seen to be at odds with our half beamwidth criterion (23) for the rotation allowed during the integration time. However, tests indicated no loss of signal strength when the azimuth bin was increased from lower values up to 15°. Still, as there must be some dependence of the signal strength on the selected azimuth bin size, we should regard the sensitivity coefficients α derived here as somewhat tentative. As discussed in section 2, the integration affects only the signal strength; the spectral shape is not affected.

3. The accumulated N pulse average is normalized by the estimate of the average power $W_0(x, \Phi)$ for each 15° azimuth bin and unity is subtracted. The data are then rewindowed by a cosine-squared (Hanning) window. In the high altitude range (8–10 km) the window end points are taken to be $x = 800$ m and $x = 3872$ m, and at the low altitudes (4–6 km) these values are halved. The midpoint of the window corresponds roughly to $\theta = 13.5°$.

4. Estimates of $P_N(K, \Phi)$ for each 15° azimuth block are computed using a 256-point fast Fourier transform. These estimates are then averaged over the several rotations of the antenna (6–40 turns).

The average power computation step is perhaps the most critical of the data processing steps, mainly on account of the antenna pattern anomaly. The average power data here have been estimated somewhat crudely: with the motion compensation disabled, the backscattered power data for each 15° azimuth bin are averaged in 96-m (eight-bin) range intervals (high-altitude data); these averages are then further averaged over the successive rotations of the antenna (6–40 turns). The resultant average power profile data are then linearly interpolated between the 96 m range bins to yield a smoother estimate of the average power envelope for each 15° azimuth bin. A final smoothing is accomplished by averaging the average power profile data W_0 over adjacent azimuth bins with a three point (0.25, 0.50, 0.25) running smoother. As mentioned above, the average power envelope so estimated may differ from the actual "instantaneous" average power profile for each individual turn because of slight aircraft attitude variations shifting the gain pattern on the surface. This shifting results in an improper registration of the computed average power envelope with respect to the actual power profile for a given turn. Since the gain pattern anomaly is about 3° in elevation, aircraft attitude variations of a few degrees can smooth out the antenna pattern anomaly in the average power estimate; the modulation spectra may then suffer some contamination for wavelengths corresponding to the 3° ripple (ca. 400 m at 10 km altitude) and longer.

In the normalization process, in order to avoid division by small numbers at the ends of the range record, a threshold is prescribed for the average power below which the average power estimates are simply set equal to the threshold value. Since the length of range record subject to the thresholding is small, and the affected record lies near the endpoints where the Hanning window is near zero, the effect of the thresholding on the derived spectra is generally small. The 3-dB width of the Hanning window is 1.44 transform bins [*Harris*, 1978]. The wave number resolution is accordingly

$$\delta K = 1.44/3072 \text{ m} = 4.7 \times 10^{-4} \text{ cpm} \tag{26}$$

for the high-altitude data (8–10 km) and double this value for the low-altitude data (4–6 km).

Figures 8*a*–8*f* are polar contour plots of the processed directional spectra $P_{42}^*(K, \Phi)$ in units of meters where $P_N^* \equiv 4\pi P_N$ is the one-sided (in K) spectrum as a function of wave number in cycles per meter. The noise background has not been subtracted in these plots, but as the snr is quite high (+10–20 dB), the background noise level is insignificant. Thus, these spectra can be viewed as directional slope spectra (one need only supply the "calibration constant" α). Figure 8*a* is the directional spectrum of a storm sea, significant wave height $H_s = 9.4$ m, dominant wavelength = 330 m. This spectrum (tape 36/file 1) was produced from a long run (40 turns), and hence it is very stable. Figures 8*b* and 8*e* are examples of bimodal spectra. Figure 8*c* represents a fairly low sea state ($H_s = 1.9$ m). The "rattiness" of this spectrum is characteristic of broadly spread directional spectra from short files (six rotations). Figure 8*f* is an interesting example. It is the observed spectrum of a unidirectional, ~330 m narrowband swell running under fairly light winds. Visually, from the vantage point of 8.4 km, the sea surface had the striking appearance of a diffraction grating, with the crest length appearing practically infinite (>40 km). If it is assumed that the swell in Figure 8*f* is indeed unidirectional and monochromatic, then it follows that the spectrum would consist of a symmetrical pair of delta functions; the observed spectrum in Figure 8*f* would then represent the spectral window, or system spectral response function. According to (2) and (26) the directional and wave number resolutions for this 330-m wave are 30° and 4.7×10^{-4} cpm. The observed half power directional dispersion in the spectrum is close to the 30° resolution; however, the observed wave number dispersion is somewhat larger than the resolution, approximately 7×10^{-4} cpm ($\delta f \cong 0.008$ Hz). This may be due to the actual finite bandwidth of the spectrum. From the buoy data (Table 1), one sees a narrow band swell at the radar-indicated frequency of 0.07 Hz; however, with the 0.01 Hz buoy resolution it can only be estimated that the bandwidth is of the order of 0.01 Hz.

The antenna pattern contamination, forming a pedestal at dc, is apparent in all the directional spectra of Figure 8. That this low-frequency contamination is indeed antenna-pattern related is evident from the factor-of-2 scaling with altitude of the pedestal width between the high-altitude spectra and the low-altitude case, Figure 8*d*.

Lastly, respecting Figure 8, we note the asymmetry that is evident in several of the spectra. This appears to be related to asymmetry in the wave-slope distribution. What is significant here is that the asymmetry is by and large rather small, and this would indicate that, by and large, the second-order hydrodynamic effects are small.

Figure 9 is a series of wave number cuts through the direc-

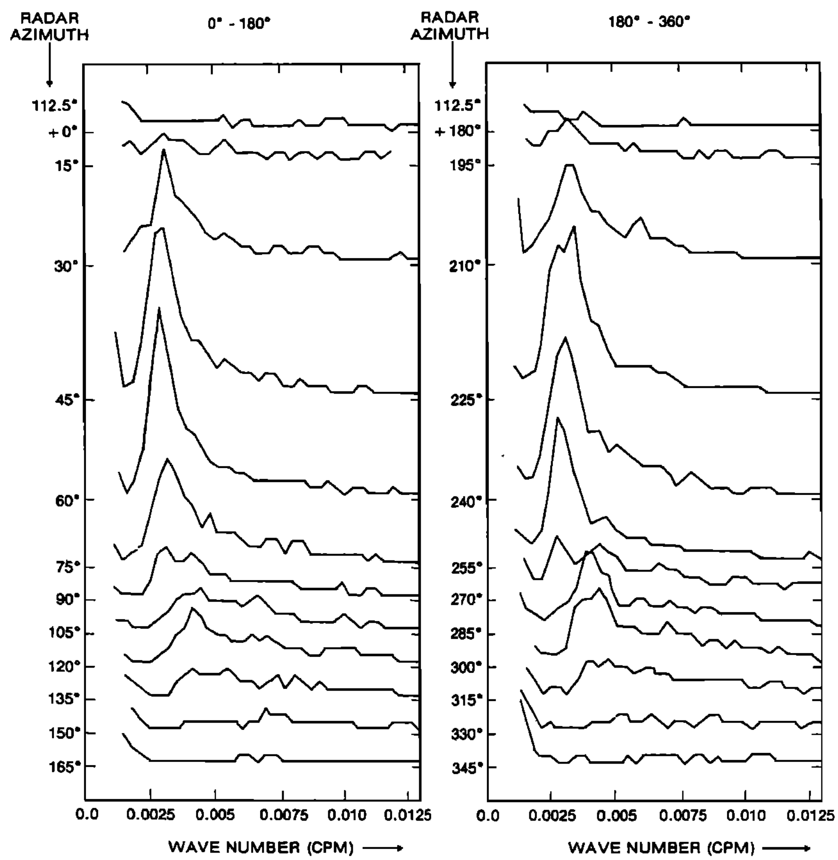

Fig. 9. Radial cuts through the directional spectrum of Figure 8a.

tional spectrum $P_N(K, \Phi)$ of Figure 8a. The figure is intended to show that the forward face of the (slope) spectrum is quite sharply defined, despite the low-frequency contamination. The spectral density between the dc pedestal and the peak (in the peak direction) amounts to only a few percent of the peak value. Thus, the directional spectrum (at least in this high sea state case) is relatively "clean" in the forward face region. However, since the low-frequency energy is relatively isotropic it can have a significant cumulative effect in the nondirectional spectrum computed simply by an integration over all directions. While the low-frequency contamination could be removed in the directional spectrum prior to the directional integration by a number of arbitrary means, we have neglected to do so here. Thus, in the nondirectional spectra to be presented, it will be seen that the low-frequency contamination is significant in the forward face region of the spectra.

4.3. *Absolute Nondirectional Comparisons*

For these comparisons, we will need to take a closer look at the residual fading spectrum which must be subtracted from P_N to give the directional modulation spectrum P_m. Because of the nonlinear time-delay versus surface range relationship (25) that obtains in the aircraft geometry, the formula (18) for P_w will not be exact. The pulse spectrum in the surface wave number domain will be similar to the pulse spectrum only when there is a linear relationship between surface range and delay time. Nevertheless, (18) may stand as a fair approximation. If we assume as a nominal range resolution the resolution at 13.5° incidence, i.e., $\Delta x = 8.14$ m, then (18) gives (with $N = 42$),

$$\frac{4\pi P_w}{N} = 0.58\ [\mathrm{m}]\ \exp\left[-0.5(K/0.033)^2\right] \qquad (27)$$

where K is given in cpm. Figure 10 is a plot of the azimuthally integrated value of P_N in the wave number band 0.0218–0.025 cpm (center frequency = 0.19 Hz) for several files, where the

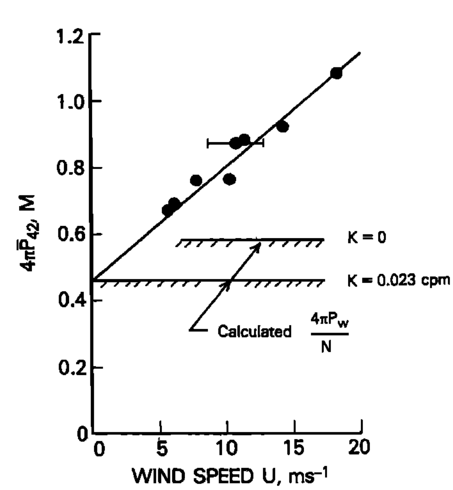

Fig. 10. Estimation of the background fading noise level. The level of the azimuthally averaged directional spectrum in the wave number band 0.0218–0.0250 cpm for 12 files is plotted versus buoy-observed wind speed. The data from the adjacent files 45/2 and 3, 86/4 and 6, 89/2 and 3, and 90/7 and 9 have been averaged together. An eyeball extrapolation to zero wind speed yields the value of the residual fading variance spectrum predicted by equation (27).

TABLE 2. Measured Versus "Theoretical" Sensitivity Coefficient

Radar Tape/File	Low-Frequency Cutoff f_c, Hz	Measured $\sqrt{\alpha}H_s$	Buoy H_s, m	α_{meas}, m^{-1}	Inferred $\langle\lvert\nabla\zeta\rvert^2\rangle$	α_{theo}, m^{-1}	Inferred H_s, m	Altimeter Mode H_s, m
36/1	0.055	10.90	9.4	1.34	0.061	1.36	9.35	...
45/2	0.070	4.55 } 4.47	3.1, 2.8 } 2.95	1.64	0.041	2.27	2.97	2.52
45/3	0.067	4.39	2.3					
85/10	0.080	4.16	2.2	3.58	0.030	3.42	2.25	2.31
86/4	0.090	3.72 } 3.80	1.9	4.00	0.028	4.57	1.78	...
86/6	0.085	3.86						
89/2	0.090	4.87	3.1[a]	2.47	0.039 } 0.041	2.48[b]	3.09	3.1[a]
89/3	0.085	6.86		4.90	0.042	5.12[b]	3.03	...
91/6	0.060	6.29	4.2	2.24	0.044	1.92	4.54	4.78
94/2	0.055	6.38	4.0	2.74	0.041	2.81	3.80	3.66

Mean $\Delta H_s = 0.00$ m; rms $\Delta H_s = 0.16$ m.
[a] H_s with energy below f_c subtracted ($\Delta H_s = -0.2$ m).
[b] Average wind speed of 10.9 ms^{-1} assumed.

buoy-observed wind speed is used as an ordering parameter. From the plot one sees that an extrapolation of the observed P_N to zero wind speed (and hence, presumably, to zero modulation depth) yields the value of the residual fading variance predicted by (27).

With P_m computed from P_N by subtracting (27), the directional height-frequency spectrum $S(f, \Phi)$ is computed using the tilt model solution (8). (Note: The data to be presented here have not been corrected for the finite pulse response $R(K)$. This correction amounts to +20% at 0.20 Hz (40-m wavelength)). Assuming the linear, deep-water dispersion relationship, it follows that

$$S(f, \Phi) = (2/\alpha f)P_m(K, \Phi) \qquad (28)$$

where S is the polar-symmetric spectrum expressed in m^2/Hz/rad. In computing (28), the measured modulation spectrum is symmetrized according to

$$P_m \leftarrow 0.5[P_m(K, \Phi) + P_m(K, \Phi + 180°)] \qquad (29)$$

Symmetrizing the spectrum has the advantage of doubling the DOF. Also, any asymmetry in the modulation spectrum which cannot be accounted for in the linear theory is eliminated. The nondirectional spectrum is now computed according to

$$\bar{S}(f) = (\alpha f)^{-1}(1/12)\sum_{i=1}^{12} 4\pi P_m(K, \Phi_i)$$
$$\equiv 4\pi\bar{P}_m(K)/\alpha f \qquad (30)$$

As pointed out before, the sensitivity coefficient α should ideally be calculated on the basis of the observed cross-section roll-off, but the poor antenna gain pattern has made this virtually impossible. Instead of estimating α directly from the average power/mean square slope data, we will make do with an indirect verification of the tilt model prediction based on the mean square slope values implied by the measured sensitivity coefficients. The measured α is taken to be the ratio of the area under the radar spectrum to the area under the buoy spectrum, namely,

$$\alpha_{meas} = \frac{\int_{f_c}^{0.2\ \mathrm{Hz}} 4\pi\bar{P}_m(K)\, d\ln f}{\int_{f_c}^{0.2\ \mathrm{Hz}} \bar{S}(f)\, df} \equiv \frac{\alpha H_s^2\ (\mathrm{radar})}{H_s^2\ (\mathrm{buoy})} \qquad (31)$$

where f_c is a low-frequency cutoff, and the significant wave height $H_s \equiv 4\langle\zeta^2\rangle^{1/2}$ (where the low-frequency deficit is understood). The low-frequency cutoff is chosen somewhat arbitrarily as the frequency of the minimum between the dc and the spectral peak in each nondirectional spectrum. Table 2 lists the measured alphas for 10 files, representing basically seven independent observations.

Figure 11 gives five examples of the inferred directional height spectra based on the measured alphas. Figures 12*a*–12*e* compare the inferred nondirectional spectra with buoy observations. The five examples shown are plotted autoscaled, linear-linear; they cover a range of sea states from $H_s = 1.9$ m to 9.4 m, and include a variety of spectral forms. It is seen that the agreement is generally excellent over the entire range from f_c to 0.2 Hz. The minor discrepancies that are apparent in some of these comparisons can be attributed, for the most part, to sampling variability, geophysical variability (colocation error), and antenna pattern contamination. One does not need to look for explanation in terms of second-order scattering effects. These effects are by and large so small as to be masked by the larger errors. For example, consider sampling variability. The 90% confidence interval on the buoy spectrum in Figure 12*a* is (0.6 $\bar{S}$, 1.9 $\bar{S}$). Thus, the confidence interval on the peak of the buoy spectrum is 130% of the full scale of the figure. The pattern contamination is evident in all figures, but it is most severe in the case of Figure 8*c*. In this case, both the frequency and the spectral density are low. If one examines all the figures, it would appear that the antenna-pattern-related dc component has a spectral density of about 2 m^2/Hz in the vicinity of 0.08 Hz; this would account for the apparent discrepancy in Figure 8*c*. The radar spectra are seen to exhibit a slight droop relative to the buoy data on the high-frequency side; most of this discrepancy can be explained by the pulse response which was not corrected for in these data (a +20% correction at 0.20 Hz). Of course, second-order effects may be present in these data. However, the main point is that the quality of the data is such that these effects cannot readily be discerned. Future data obtained with a better antenna pattern will be required before the second-order effects can be investigated quantitatively.

From these comparisons, we conclude that the measurements can be made with good spectral fidelity; if we can now show that the measured sensitivities as well as are consistent with the tilt model prediction, then a fairly good case can be made

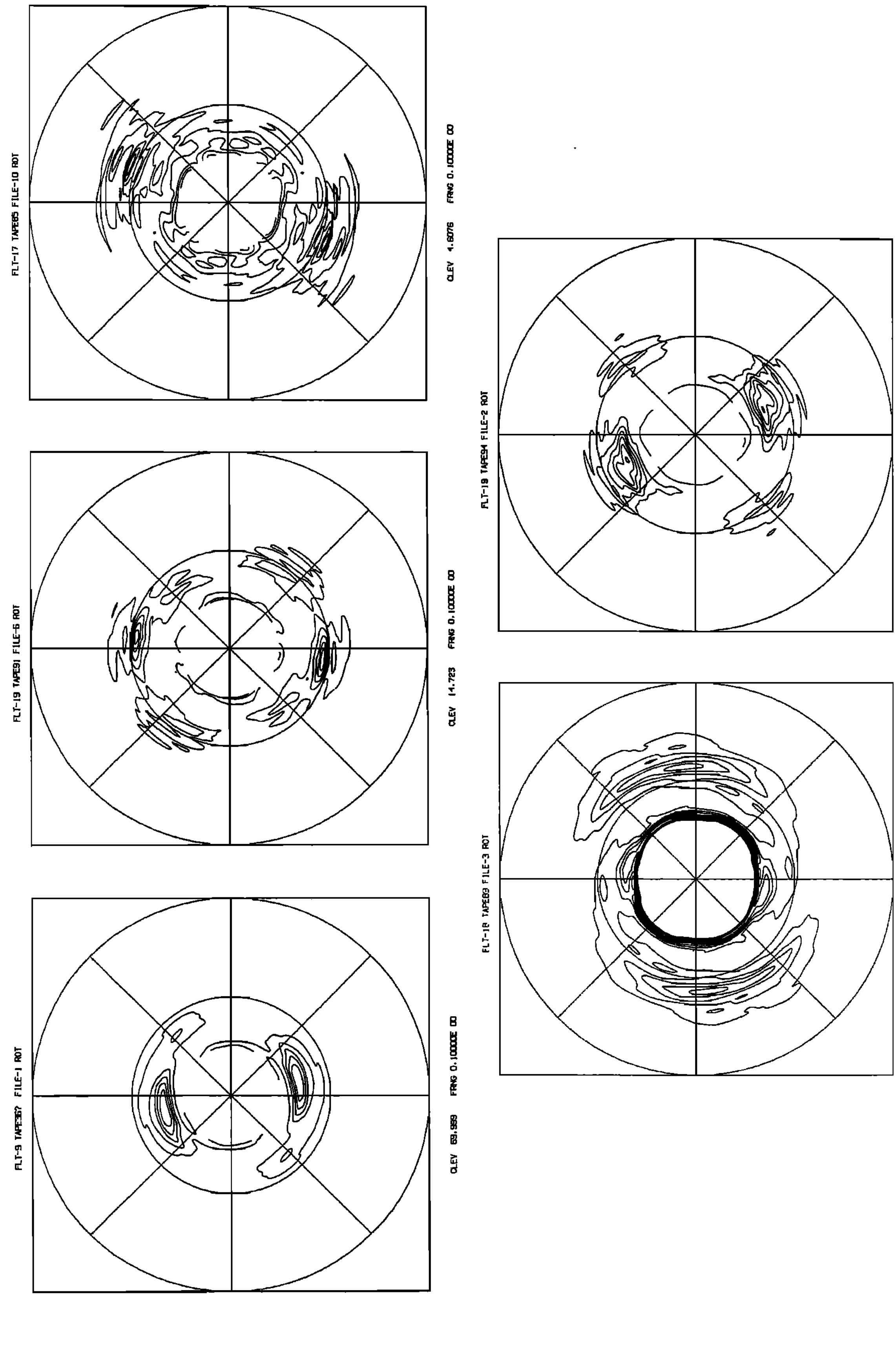

Fig. 11. Polar-symmetric directional height spectra $S(f, \Phi)$ corresponding to Figures 8a–8e. The frequency rings are 0.1 Hz and 0.2 Hz. The equally-spaced contour levels (CLEV), in units m^2/Hz/rad, have been multiplied by a factor of 2π.

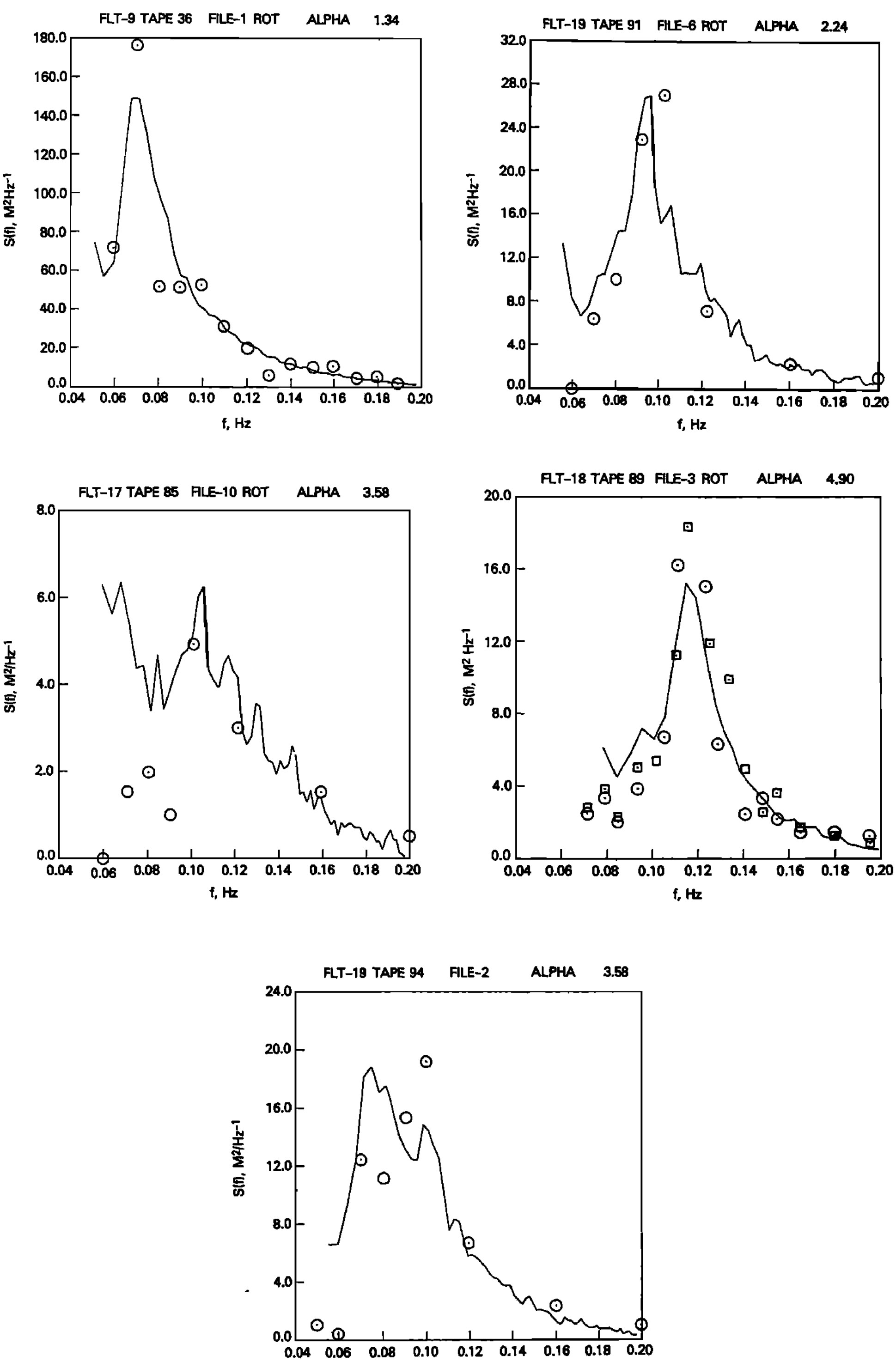

Fig. 12. Comparisons of radar-inferred (solid line) and buoy (circles) nondirectional height spectra $S(f)$ using the measured alphas. Figures 8a–8e correspond to Figures 11a–11e. In Figure 12 the circles and squares stand for the buoy records at 2138 UT and 2104 UT, respectively. The 2138 UT data have been smoothed by a 2-point average in the vicinity of the peak. The large low-frequency energy in these spectra is due mainly to antenna pattern contamination. These data have not been corrected for the finite pulse response $R(K)$. This correction is (a maximum of) +20% at 0.2 Hz.

for the overall validity of the measurement technique. First, consider the footprint ($1/L_y$) dependence in (11). This asympotic dependence can be checked by comparing files 89/2 and 89/3. The ratio of the altitudes is $9.3/4.5 = 2.07$; the ratio of the measured alphas is $4.90/2.47 = 1.98$ (a 4% difference). Thus, the inverse L_y scaling appears to be correct. Let us now check the dependence on the mean square slope by inferring mean square slope values from the measured alphas. If the inferred values are reasonable, then this would represent a confirmation of the tilt model. Assuming a nominal incidence angle of 13°, we invert (11) to obtain

$$\langle|\nabla\zeta|^2\rangle = \frac{2\tan 13°}{(L_y\alpha_{\text{meas}}/\sqrt{2\pi})^{1/2} - \cot 13°} \tag{32}$$

The inferred mean square slope values are tabulated in Table 2 and plotted in Figure 13 as a function of the buoy-observed wind speed. No corrections were made for anemometer height or atmospheric stability. An eyeball regression yields the relationship

$$\langle|\nabla\zeta|^2\rangle = 0.0028U[\text{ms}^{-1}] + 0.009 \tag{33}$$

for the wind speed range of approximately 5–20 ms^{-1}. Equation (33) agrees quite well with the K_u-band scatterometer data analyzed by *Wentz* [1977], at least up to the largest wind speed (12 ms^{-1}) in Wentz's data set. Equation (33) also agrees with *Wilheit*'s [1979] analysis of passive microwave data in predicting slope variances that are ~60% of the (clean-surface) optical values reported by *Cox and Munk* [1954]. The inferred mean square slope values (33) are thus consistent with our knowledge of what the K_u-band diffraction-effective slopes should be and strongly support our conclusion that the tilt model solution (8) is a correct first-order relationship.

Now let us use the regression result (33) in (11) to compute a "theoretical" alpha. The "theoretical" alpha can then be used to compute a "radar-inferred" absolute height spectrum and significant wave height. Table 2 is a tabulation and Figure 14 is a plot of the results for the "inferred" wave height for the seven independent cases analyzed. Over the wave height range 1.9 m to 9.4 m the mean difference between the radar-inferred and buoy H_s is 0.00 m (sic) and the rms difference is 0.16 m. This is truly remarkable considering that (1) we are using only a first-order, back-of-the envelope theory, (2) our measurement geometry is not ideal (broad elevation beamwidth), (3) we have had to rely on external parameters (buoy wind speeds) rather than internal parameters (cross-section roll-off) to compute the sensitivity coefficient, and lastly, (4) the data are subject to sampling variability as well as geophysical variability (colocation errors). Some information as to the last source of error is available to us through the instrument's altimeter mode. The altimeter mode algorithm consisted of epoch realignment, and an iterative least squares fitting of an error function to the leading edge of the average pulse return. H_s was computed from the measured temporal dispersion σ according to

$$H_s = [4c^2\sigma^2 - H_p{}^2]^{1/2} \tag{34}$$

where $H_p = 4.91$ m (compare with *Fedor et al.* [1979]). The altimeter wave heights are shown in the last column of Table 2 and are plotted in Figure 15. The altimeter H_s show a positive correlation with the spectrometer mode minus buoy H_s residuals indicating that colocation errors are a significant component of the error budget. This probably explains the discrepancy in the bimodal spectrum comparison of Figure 12e. However, there does remain the possibility that the discrepancy is due anisotropy of the sensitivity coefficient. An anisotropy in the slope pdf such as to produce a 20% anisotropy in α is quite reasonable, and would in part explain why the lower frequency (swell) component at 45° to the wind is weighted higher by the radar. Future data collected with an improved antenna pattern should help to resolve this uncertainty regarding anisotropic effects.

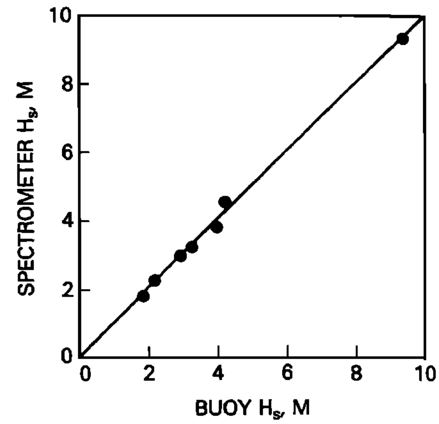

Fig. 14. Radar-inferred versus buoy significant wave height (spectrometer mode). Data from adjacent files have been averaged together; see Table 2.

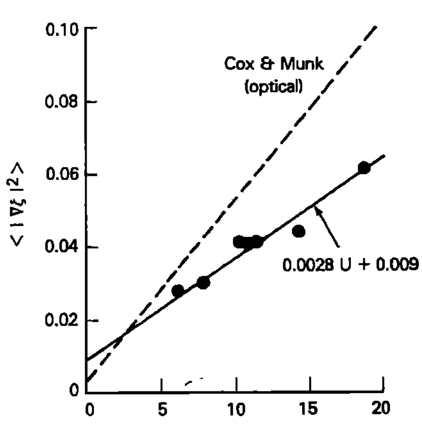

Fig. 13. Mean square slopes inferred from the measured alphas versus wind speed.

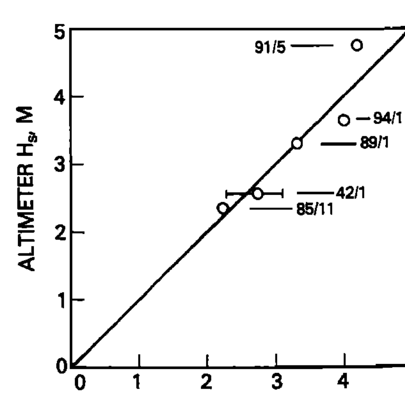

Fig. 15. Radar-inferred versus buoy significant wave height (altimeter mode).

4.4. *Directional Comparison*

The single directional comparison available to us from the fall 1978 mission (and to date the only in situ directional comparison available to us) is with a NOAA pitch-roll buoy deployed from weather station PAPA (cf. Table 1). Because of the uniqueness of these data, we have expanded upon and refined the analysis originally given in this section and made this directional comparison the subject of a companion paper [*Jackson et al.*, this issue].

5. CONCLUSION

We have described a rather simple microwave radar technique for measuring directional wave spectra. We have shown that satellite measurements on a truly global scale are possible with this technique, and we have, in our opinion, provided a firm theoretical and experimental basis for the technique. The data reported here demonstrate that accurate directional energy spectrum measurements are possible with this technique, at least for sea states in excess of 2 m and wind speeds in excess of 5 m/s or so. For lower (and steeper) sea states and lower wind speeds, one may expect some loss of measurement fidelity. For the more interesting high sea state cases it appears that the measurement fidelity (to the slope spectrum) is excellent.

The verification data presented in this report consisted entirely of nondirectional spectra. However, the directional comparison given in the companion paper [*Jackson et al.*, this issue] indicates good agreement directionally as well.

The only problem with the fall 1978 mission data (one much harped upon) was the antenna pattern anomaly caused by the baffle around the antenna. Aircraft attitude changes, unaccounted for in the data analysis, acted to shift the gain pattern and the anomalous structure so as to foil the normalization procedure. As a result, a significant amount of low-frequency antenna pattern energy contaminates the spectra reported here; the contamination is especially severe in the nondirectional height spectrum. This problem has been eliminated in recently obtained flight data with an improved antenna/radome environment and an improved average power computation which corrects for aircraft attitude variations. The new data exhibit very low levels of low-frequency energy in the inferred nondirectional height spectra (cf. *Jackson*, 1984, Figure 10). With such data one might begin to look for evidence of the second-order scattering effects investigated theoretically by *Jackson* [1981]. The new flights are being conducted not only with a better-formed off-nadir beam, but with a new lower gain nadir horn antenna that allows for a fairly accurate estimation of the cross-section roll-off and mean square slope parameter according to the method of *Hammond et al.* [1977]. These new flights are being conducted in concert with the surface contour radar [*Walsh et al.*, 1981], a 36-GHz direct topographic mapping radar. The low-flying surface contour radar (SCR) is capable of directional spectrum measurements of resolution comparable to our scanning-beam technique, and we are presently relying almost exclusively on the SCR for high-resolution directional spectrum intercomparison data for further validating and refining our radar technique.

Acknowledgments. J. E. Eckerman initiated the Goddard "Short Pulse Radar" program nearly a decade ago, and for many years he was the motivating force behind it. In 1974, he acquired the GEOS 3 breadboard altimeter and hired one of us (W. T. W.) to make a working radar of it; subsequently, he hired another of us (F. C. J.) to figure out how and why it should be working. We can only hope that the accomplishment of the present work in some measure releases us from a nontrivial debt of gratitude. The cooperation of the following individuals and institutions is also gratefully acknowledged: P. Gloersen, NASA Goddard Space Flight Center; E. Peterson, NASA Ames Research Center, and the crew of the CV-990 aircraft, the Galileo II; S. Renwick, NOAA Data Bouy Office; S. Tryggstad, director, VHL River and Harbour Laboratory, Trondheim, Norway; and D. Ross and W. McLeish, NOAA Atlantic Oceanographic and Meteorological Laboratories, Miami, Florida. We thank T. Wilheit for a helpful suggestion; also, the contributions of J. McArthur, Applied Physics Laboratory, C. Y. Peng, Science Systems and Applications Inc., and K. Tolbert, Computer Sciences Corporation, are acknowledged. This work has been supported by supporting research and technology funding from the Oceanic Processes Branch of NASA Headquarters.

REFERENCES

Alpers, W., and K. Hasselmann, The two-frequency microwave technique for measuring ocean wave spectra from an airplane or satellite, *Boundary Layer Meteorol.*, *13*, 215–230, 1978.

Beal, R. C., P. S. Deleonibus, and I. Katz (Eds.), *Spaceborne Synthetic Aperture Radar for Oceanography*, 215 pp., Johns Hopkins Press, Baltimore, 1981.

Beckmann, P., and A. Spizzichino, *The Scattering of Electromagnetic Waves From Rough Surfaces*, 503 pp., Pergamon, New York, 1963.

Blackmann, R. B., and J. W. Tukey, *The Measurement of Power Spectra*, p. 21, Dover, New York, 1958.

Brown, G. S., Backscattering from a Gaussian-distributed perfectly conducting rough surface, *IEEE Trans. Antennas Propag.*, *AP-26*, 472–482, 1978.

Cox, C., and W. Munk, Measurement of the roughness of the sea surface from photographs of the sun's glitter, *J. Opt. Soc. Am.*, *44*, 838–850, 1954.

Earl, M. D., Problems in ocean wave hindcasting, in *Spaceborne Synthetic Aperture Radar for Oceanography*, edited by R. C. Beal, P. S. Deleonibus, and I. Katz, 215 pp., John Hopkins Press, Baltimore, 1981.

Fedor, L. S., T. W. Godbey, J. F. R. Gower, R. Guptill, G. S. Hayne, C. L. Rufenach, and E. J. Walsh, Satellite altimeter measurements of sea state: An algorithm comparison, *J. Geophys. Res.*, *84*, 3991–4002, 1979.

Hammond, D. L., R. A. Mennella, and E. J. Walsh, Short pulse radar used to measure sea surface wind speed and SWH, *IEEE Trans. Antennas Propag.*, *AP-25*, 61–67, 1977.

Harris, F. J., On the use of windows for harmonic analysis with discrete Fourier transforms, *Proc. IEEE*, *66*(1), 51–83, 1978.

Hasselmann, K. (Ed.), Sea wave modelling project report, in *Proceedings of Symposium on Wave Dynamics and Radio Probing of the Ocean Surface*, Plenum, in press, 1984.

Huang, N. E., and S. R. Long, An experimental study of the surface elevation probability distribution and statistics of wind-generated waves, *J. Fluid Mech.*, *101*, 179–200, 1980.

Jackson, F. C., The reflection of impulses from a nonlinear random sea, *J. Geophys. Res.*, *84*(C8), 4939–4943, 1979.

Jackson, F. C., An analysis of short pulse and dual frequency radar techniques for measuring ocean wave spectra from satellites, *Radio Sci.*, *16*, 1385–1400, 1981.

Jackson, F. C., Some case studies of ocean wave physical processes utilizing the GSFC radar ocean wave spectrometer, Proceedings of URSI Commission F Symposium and Workshop on Frontiers of Remote Sensing of the Oceans and Troposphere, Shoresh, Israel, May 14–23, 1984, *NASA Conf. Publ.*, *2303* 233–246, 1984.

Jackson, F. C., W. T. Walton, and C. Y. Peng, A comparison of in situ and airborne radar observations of ocean wave directionality, *J. Geophys. Res.*, this issue.

Johnson, J. W., W. L. Jones, and D. E. Weissman, Two-frequency (Δk) microwave scatterometer measurements of ocean wave spectra from an aircraft, in *Oceanography from Space*, edited by J. F. R. Gower, pp. 607–616, Plenum, New York, 1981.

Jones, W. L., L. C. Schroeder, and J. L. Mitchell, Aircraft measurements of the microwave scattering signature of the ocean, *IEEE J. Oceanic Eng.*, *OE-2*, 52–61, 1977.

Levine, D. M., W. T. Walton, J. Eckerman, R. L. Kutz, M. Dombrowski, and J. E. Kalshoven, Jr., GSFC short pulse radar, JONSWAP-75, *NASA Tech. Note, TN D-8502*, 42 pp., 1977.

Plant, W. J., W. C. Keller, and D. E. Weissman, The dependence of X-band microwave sea return on atmospheric stability and sea state, *J. Geophys. Res.*, in press, 1985.

Tomiyasu, K., Short pulse wide-band scatterometer ocean surface signature, *IEEE Trans. Geosci. Electron., GE-9*, 175–177, 1971.
Townsend, W. F., An initial assessment of the performance of the Seasat-1 radar altimeter, *IEEE J. Oceanic Eng., OE-5*, 80–92, 1980.
Valenzuela, G. R., Theories for the interaction of electromagnetic and ocean waves—A review, *Boundary Layer Meteorol., 13*, 61–85, 1978.
Walsh, E. J., D. W. Hancock, III, D. E. Hines, and J. E. Kenney, Surface contour radar remote sensing of waves, in *Directional Wave Spectra Applications*, edited by R. L. Wiegel, pp. 281–298, American Society of Civil Engineers, New York, 1981.
Wentz, F. J., A two-scale scattering model with application to the JONSWAP '75 aircraft microwave scatterometer experiment, *NASA Contract. Rep., CR-2919*, 124 pp., 1977.
Wilheit, T. T., The effect of wind on the microwave emission from the ocean surface at 37 GHz, *J. Geophys. Res., 84*, 4921–4926, 1979.

P. L. Baker, Computer Technology Associates, 7927 Jones Branch Road, McLean, VA 22102.
F. C. Jackson, Laboratory for Oceans, NASA Goddard Space Flight Center, Code 671, Greenbelt, MD 20771.
W. T. Walton, Engineering Research Center, University of Maryland, College Park, MD 20742.

(Received July 27, 1984;
accepted August 8, 1984.)